

Electronic Supplementary Information

Linking Atomic to Mesoscopic Scales in Multilevel Structural Tailoring of Single-Atom Catalysts for Peroxide Activation

Li Yu,* Shaosong Xin, Yuchan Li, and Hsien-Yi Hsu

Supplementary Figures

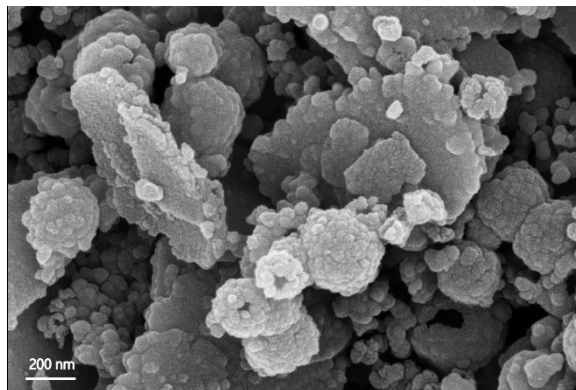


Fig. S1 A SEM image of Fe–N doped carbon with coexisting irregular polymerized particles due to excessively fast dissolving-out of Fe_3O_4 and Py polymerization.

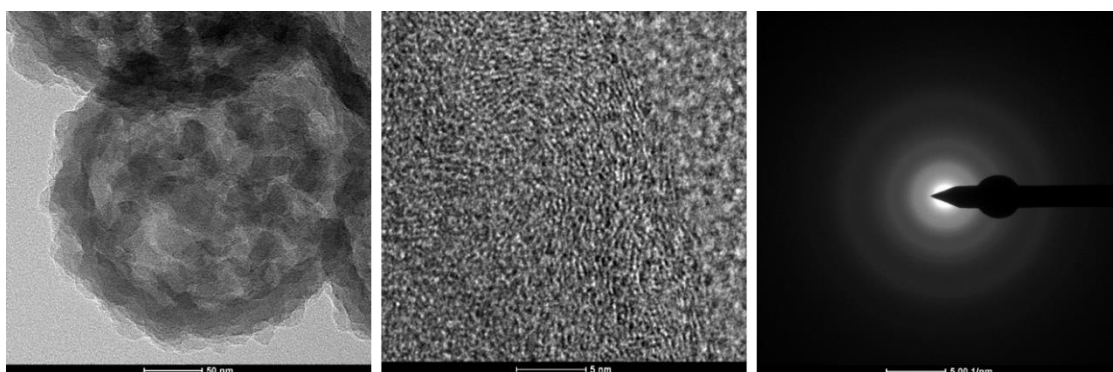


Fig. S2 TEM and SAED images showing the porous structured P-FeNOSAC that was synthesized under a decreased concentration of acid and a reaction of 5 h.

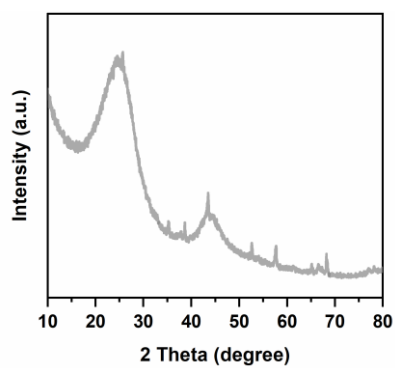


Fig. S3 XRD patterns showing the presence of iron carbide phases, when V_{dis} was too low during the synthesis.

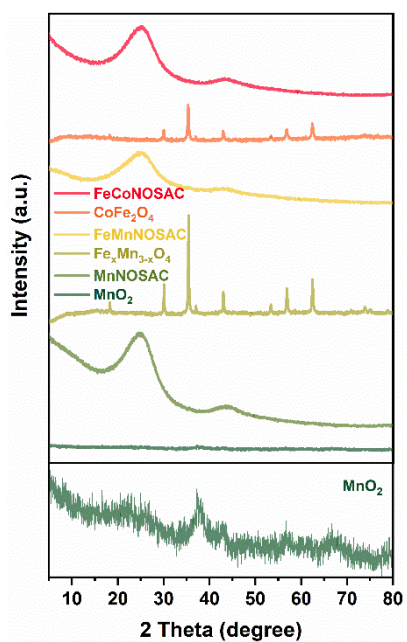


Fig. S4 XRD patterns revealing the conversion of metal oxides to the corresponding SACs. An enlarged version of the XRD pattern for MnO₂ is provided below for visibility.

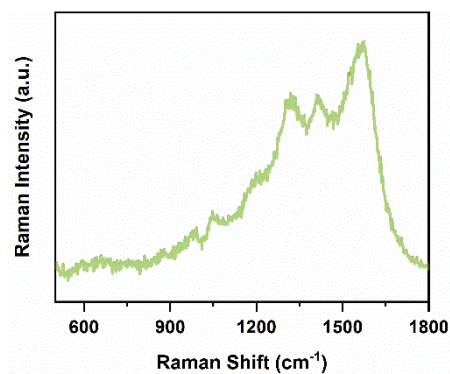


Fig. S5 Raman spectrum of Fe-PPy and the assignment of the Raman spectral bands as follows.

Position (cm⁻¹)	Assignment
878	$\nu(\text{C}-\text{C})$ ring deformation
980	$\nu(\text{C}-\text{C})$ ring in-plane deformation
1050	Symmetric $\nu(\text{C}-\text{H})$ in-plane bending and $\nu(\text{N}-\text{H})$ in-plane deformation
1230	$\nu(\text{C}-\text{H})$ antisymmetric in-plane bending
1319	$\nu(\text{C}-\text{C})$ in-ring
1410	$\nu(\text{C}-\text{C})$ inter-ring stretch
1575	$\nu(\text{C}-\text{C})$ $\nu(\text{C}-\text{N})$ stretch $\nu(\text{C}=\text{C})$ in-ring and $\nu(\text{C}-\text{C})$ inter-ring stretch in the backbone

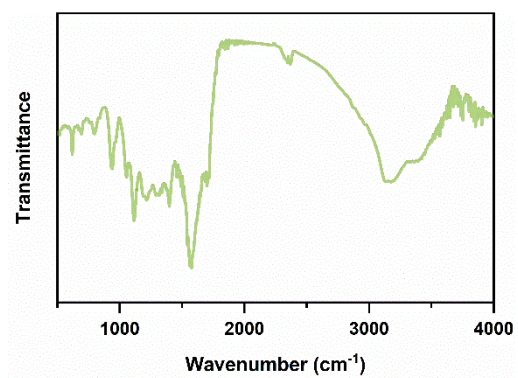


Fig. S6 FTIR spectrum of Fe-PPy.

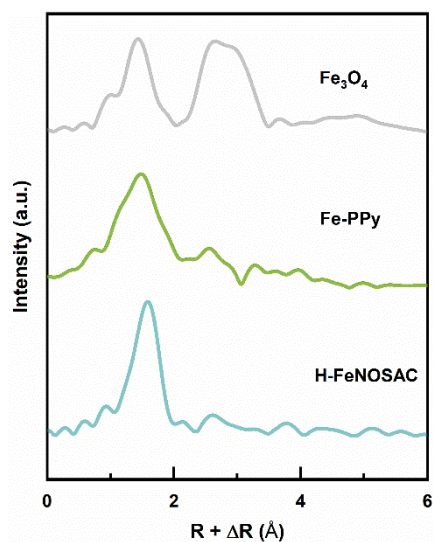


Fig. S7 Fourier transforms of k^3 -weighted $\chi(k)$ function of the Fe K -edge EXAFS spectra.

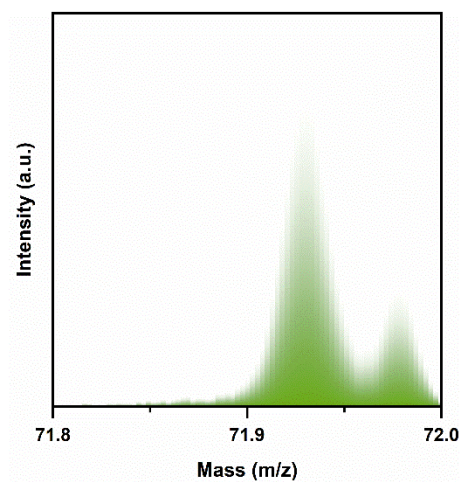


Fig. S8 ToF-SIMS analysis in the characteristic fragment yields of FeO^+ .

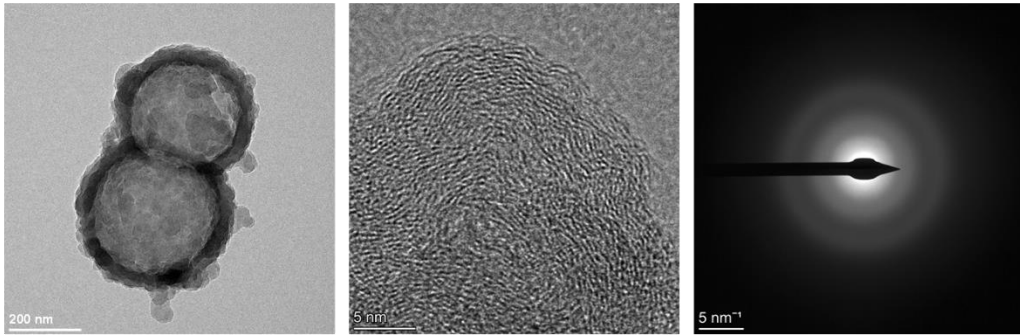


Fig. S9 TEM and SAED images showing the hollow-structured H-FeNSAC.

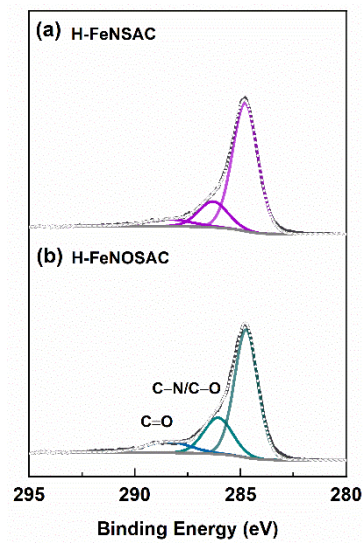


Fig. S10 High resolution C 1s XPS profiles.

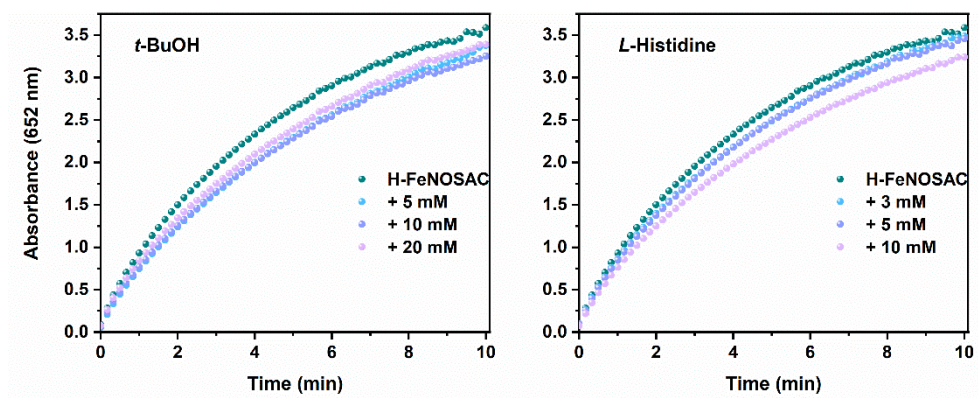


Fig. S11 Reaction-time curves in the presence and absence of *tert*-butanol and *L*-histidine.

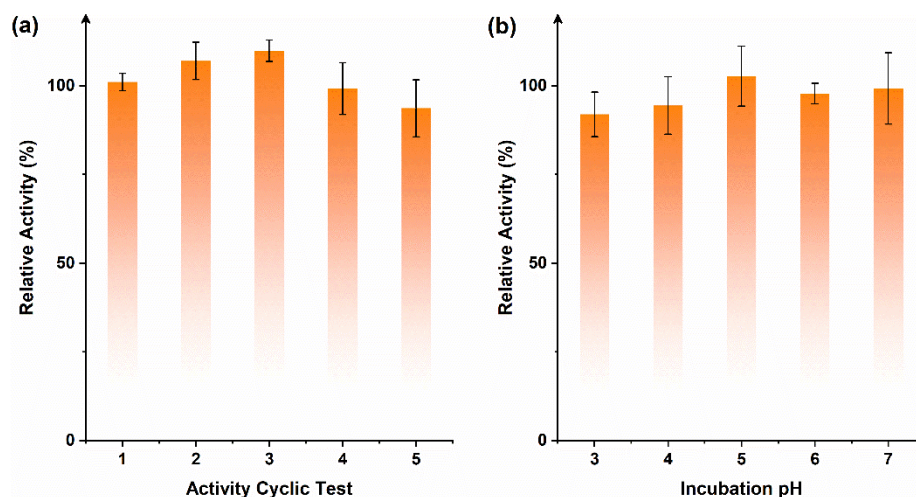


Fig. S12 Catalytic stability and activity robustness of H-FeNOSAC. (a) Cycling tests conducted to investigate the reusability of H-FeNOSAC for hydrogen peroxide activation. (b) Activity assessment after pH incubation: H-FeNOSAC was incubated at different pH levels, followed by testing its activity for hydrogen peroxide activation under standard conditions. The relative activity was normalized to the value obtained in the initial standard test.

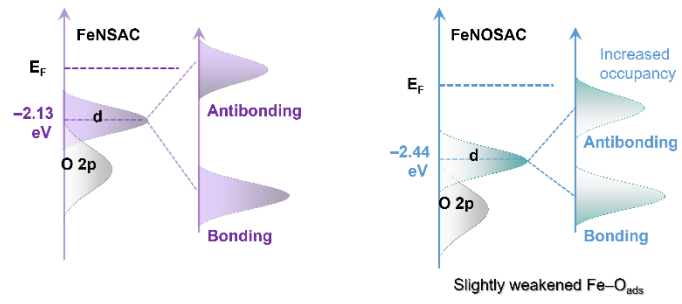


Fig. S13 Schematic comparison of the energy level and d -band centers.

Supplementary Tables

Table S1 Curve fitting parameters in the EXAFS simulation (N , coordination number; R , absorber-backscatter distance; σ^2 , Debye-Waller factor; ΔE , energy shift; R -factor).

Sample	Path	N	R (Å)	σ^2 (10^{-3} Å ²)	ΔE (eV)	R -Factor (%)
H-FeNSAC	Fe-N	3.9	1.94	3.2	4.9	0.7
H-FeNOSAC	Fe-N	2.1	1.91	4.3	7.6	1.2
	Fe-O	1.9	2.00	4.3		

Supplementary Methods

Synthesis of Fe₃O₄, Fe_xMn_{3-x}O₄, and CoFe₂O₄ Nanospheres. A modified solvothermal method was used for synthesis of Fe₃O₄ nanospheres.¹ Specifically, iron(III) chloride hexahydrate (1.35 g) and ammonium acetate (3.85 g) were dissolved in 75 mL of ethylene glycol under vigorous stirring. Afterwards, this homogeneous mixed solution was transferred to a Teflon-lined autoclave and solvothermally treated at 200 °C for 10 h. The collected products were repetitiously washed with ethanol and finally vacuum-dried at 60 °C. Manganese(II) chloride tetrahydrate (0.495 g) and iron(III) chloride hexahydrate (0.675 g) were used as the metal precursor for Fe_xMn_{3-x}O₄, while cobalt(II) chloride hexahydrate (0.4 g) and iron(III) chloride hexahydrate (0.9 g) were used for CoFe₂O₄.

Synthesis of MnO₂ Nanospheres. The MnO₂ nanospheres were obtained via a KMnO₄-engaged redox reaction under ambient conditions.² Briefly, 4.4 mL of *n*-butanol and 9.2 mL of butyric acid were completely dissolved in 100 mL of ultrapure water. The other 100 mL of aqueous solution containing 0.632 g of KMnO₄ was poured into the above solution under vigorous stirring for 30 min. The yielded precipitate was isolated by vacuum filtration and ultrasonically washed with ethanol and water for several times. After thorough drying, the products were further calcined at 300 °C for 2 h in a muffle furnace.

Multilevel Structural Tailoring of SACs. The synthesis of SACs began with an *in-situ* polymerization of Py on the corresponding metal oxides. Further pyrolysis treatments allowed the transformation of the obtained metal-containing polymers into SACs. For the synthesis of MnNOSAC and FeNOSAC hollow structures, 0.15 g of MnO₂ or Fe₃O₄ was first ultrasonically dispersed in 20 mL of ethanol solution containing 1 mL of Py. After sonication for 1 h, 80 mL of aqueous hydrochloric acid solution (1 M) was added to initiate the dissolution of metal oxides and the simultaneous polymerization. The reaction lasted for 3 h under ambient conditions and sonication. The products were harvested by vacuum filtration, washed several times and vacuum-dried at 60 °C, before pyrolysis at 800 °C for 1 h in nitrogen atmosphere. To synthesize FeMnNOSAC and FeCoNOSAC, a similar method was employed except for the use of Fe_xMn_{3-x}O₄ and CoFe₂O₄, respectively as the metal oxide template. The Fe₃O₄ derived reference SACs were obtained by varying the acid concentration and/or reaction time. Specifically, H-FeNSAC was synthesized in a similar way to the synthetic method of H-FeNOSAC, except for a prolonged reaction of 5 h to ensure the complete dissolution of metal oxide. In this way, the dissolved Fe exclusively interacted with the polymer to form Fe–N coordination. P-FeNOSAC was obtained under a decreased acid concentration of 0.5 M and a reaction of 5 h. For comparison, N-doped hollow carbon nanosphere (C_{PPy}) was prepared by pyrolysis of metal-free PPy after acid-leaching of Fe-PPy to remove the residual Fe.

Physicochemical Characterizations. The morphologies and microstructures were investigated on a ZEISS Merlin Compact field-emission SEM, and a JEOL JEM-2100F HRTEM equipped with a Bruker EDX to map the elemental distribution of the samples. Atomic resolution imaging was achieved on a spherical aberration corrected JEOL JEM-ARM200F electron microscopy under a HAADF-STEM mode. The crystal structures and chemical composition were characterized by powder XRD (Panalytical X'Pert Pro MPD diffractometer), FTIR (Nicolet 5700), confocal Raman microspectroscopy (LabRAM HR Evolution, HORIBA Jobin Yvon), and XPS (ESCALAB250Xi, Thermo Scientific) with a mono-chromatic Al K α source. Nitrogen adsorption-desorption isotherms were collected at liquid nitrogen temperature on a gas adsorption analyzer instrument (ASAP 2020 HD88, Micromeritics). The pore size distribution of the micropore, mesoporous and macropore were calculated from the adsorption branch of the isotherms, based on a non-

linear density functional theory (NL-DFT) and Barrett-Joyner-Halenda (BJH) methods. The XAFS investigations were performed in fluorescence mode at the BL14W1 beamline of Shanghai Synchrotron Radiation Facility (SSRF). The k^3 -weighted $\chi(k)$ function was Fourier-transformed into R-space to compare the contribution of each bond pair to the EXAFS oscillation peaks. *In-situ* EPR was employed to detect reactive oxygen species with a Bruker model A300-10/12 spectrometer operating at room temperature. Before determining metal contents of the SACs by ICP-OES (Optima 8300, PerkinElmer), the pretreatment of catalysts at 600 °C in muffle was conducted to completely remove the carbon. The resulting products were dissolved in ultrapure nitric acid at 80 °C, followed by dilution with ultrapure water before measurements.

The surface compositions of the samples were analyzed using a ToF-SIMS V time-of-flight secondary ion mass spectrometer (ION-TOF GmbH, Münster). The instrument is equipped with a 30-keV bismuth liquid metal ion gun (LMIG) and a 20-keV argon gas cluster ion source as primary and sputter ion sources, respectively. Both sources were angled at 45° to the sample surface. An electron flood gun was used to neutralize charge buildup. The secondary ions of the same polarity were sent to a two-stage reflectron time-of-flight mass analyzer and detected by a pair of microchannel plates with a time-to-digital converter. All measurements were taken in positive-ion modes with high signal intensity and mass resolution. The spectra were collected in dual beam mode with Ar_n^+ cluster ions as sputter species and Bi^+ as primary ions. To avoid surface oxidation and other sputtering-induced structural alterations, the sputter ion source (Ar_n^+ , 10 keV, 9 nA, $100 \times 100 \mu m^2$) was set to a sputtering rate of 1.87 nm/s (equivalent to SiO_2). The primary ion source (Bi^+ , $200 \times 200 \mu m^2$) used a bunched beam with a time-averaged pulsed primary ion current of 0.8 pA, a pulse width of less than 1 ns, and a cycle time of 150 μs . The typical probe size of the Bi^+ LMIG was approximately 5 μm . The mass scale was calibrated internally using easily identifiable secondary ions ($C_2H_5^+$, $C_3H_7^+$, and $C_4H_9^+$). The mass resolutions (measured at $C_2H_3^+$, m/z 27) were usually greater than 6000. The spectral acquisition dose was between 10^{11} and 10^{12} ions/cm² for positive ion spectra.

POD-Like Activity Evaluation and Kinetics Assay. The POD-like activity of the synthetic materials was determined by recording the absorbance of oXTMB in the presence of H_2O_2 .³ In a typical procedure, the tested nanozymes were introduced into sodium acetate buffer solution (0.2 M, pH 4.0) containing 0.48 mM of TMB and 0.6 M of H_2O_2 . All the reactions were performed in colorimetric tubes with a total volume of reaction mixture of 2.5 mL at room temperature. After the substrates were mixed, the reaction progress was immediately tracked by following the increase in absorbance at 652 nm in a time-scan mode. Reaction-time curves of the TMB colorimetric reaction were obtained by plotting the absorbance versus reaction time. Absorbance was given by subtracting the background absorbance from the nanoparticle suspension and was converted to product concentration by the Beer-Lambert Law. Initial reaction rate (V) was determined from the initial linear part of the reaction-time curve. To quantify the nanozyme activity, the tested nanozyme suspensions were supplemented in different concentrations and the specific activities ($U\ mg^{-1}$) were calculated from the corresponding plots of nanozyme activities against weights. Steady-state kinetic assays were performed by varying the substrate concentration of TMB. Apparent kinetic parameters for nanozyme activity were extracted from Michaelis-Menten equation by least squares fitting the data of the initial reaction rates and substrate concentrations.

Computational Method. The first-principle calculations in the framework of density functional theory (DFT) were performed based on the Perdew-Burke-Ernzerhof (PBE) exchange-correlation functional within the generalized gradient approximation (GGA). The ionic cores were described with the projector augmented wave (PAW) method.⁴⁻⁸ A plane-wave basis-set energy cutoff of 400 eV was used in the calculation. All

calculations were continued until the total energy and ionic force converged to less than 10^{-5} eV and 0.01 eV/Å, respectively. The interlayer distance along the z direction was set to be 15 Å by inserting a vacuum slab to alleviate undesired self-interactions between the two neighboring images. The adsorption energy E_{ads} was defined as $E_{\text{ads}} = E_{\text{sa}} - (E_{\text{cs}} + E_{\text{a}})$, where E_{sa} , E_{cs} and E_{a} are the total energy of substrate with adsorbates in its equilibrium geometry, the total energy of the clean substrate and the total energy of the free adsorbates, respectively. The barrier (E_{b}) and reaction energy (ΔE) were calculated according to $E_{\text{b}} = E_{\text{TS}} - E_{\text{IS}}$ and $\Delta E = E_{\text{FS}} - E_{\text{IS}}$, where E_{IS} , E_{TS} and E_{FS} are the total energy of its initial state (IS), transition state (TS) and final state (FS), respectively.

Supplementary References

1. H. Deng, X. Li, Q. Peng, X. Wang, J. Chen and Y. Li, *Angew. Chem. Int. Ed.*, 2005, **44**, 2782-2785.
2. S. Ching, I. J. Richter, K. A. Tutunjian, D. A. Kriz and Y. Kovic, *Chem. Commun.*, 2015, **51**, 1961-1964.
3. B. Jiang, D. Duan, L. Gao, M. Zhou, K. Fan, Y. Tang, J. Xi, Y. Bi, Z. Tong, G. F. Gao, N. Xie, A. Tang, G. Nie, M. Liang and X. Yan, *Nat. Protoc.*, 2018, **13**, 1506-1520.
4. P. E. Blöchl, *Phys. Rev. B*, 1994, **50**, 17953-17979.
5. G. Kresse and J. Furthmüller, *Comput. Mater. Sci.*, 1996, **6**, 15-50.
6. G. Kresse and J. Furthmüller, *Phys. Rev. B*, 1996, **54**, 11169-11186.
7. J. P. Perdew, K. Burke and M. Ernzerhof, *Phys. Rev. Lett.*, 1996, **77**, 3865-3868.
8. G. Kresse and D. Joubert, *Phys. Rev. B*, 1999, **59**, 1758-1775.